Article

Tuning the Mechanical and Antibacterial Properties of ZrO_2 Thin Films by Varying Deposition Angle and Orientation for Biomedical Applications

Asma Gzaiel [1,2,3], Khalil Aouadi [3,4], Aurélien Besnard [5,*], Yoann Pinot [1], Corinne Nouveau [1], Faker Bouchoucha [2], Yahya Agzenai Ben Salem [6], Amina Guessabi [7] and Boudjemaa Bouaouina [8]

[1] Arts et Metiers Institute of Technology, LaBoMaP, F-71250 Cluny, France; asma.ghzaiel@ensam.eu (A.G.); yoann.pinot@ensam.eu (Y.P.); corinne.nouveau@ensam.eu (C.N.)
[2] Research Laboratory LR-18ES45 Physics, Mathematics, Quantum Modeling and Mechanical Design, University of Carthage, IPEIN, Nabeul 8000, Tunisia; fakersbouchoucha@yahoo.fr
[3] Tunisia Polytechnic School, BP. 743, La Marsa 2078, University of Carthage, Tunis 1080, Tunisia
[4] Engineering and Durability of Materials Center, Moroccan Foundation for Advanced Science, Innovation and Research (MASCIR), University Mohammed VI Polytechnic, Lot 660, Hay Moulay Rachid, Ben Guerir 43150, Morocco; khalil.aouadi@um6p.ma
[5] Université Marie et Louis Pasteur, SUPMICROTECH, CNRS, Institut FEMTO-ST, F-25000 Besançon, France
[6] High Throughput Multidisciplinary Research Laboratory (HTMR), College of Chemical Sciences and Engineering (CCSE), Mohammed VI Polytechnic University (UM6P), Ben Guerir 43150, Morocco; yahya.agzenaibensalem@um6p.ma
[8] Plant and Microbial Biotechnology, Moroccan Foundation for Advanced Science, Innovation and Research (MASCIR), Mohammed VI Polytechnic University (UM6P), Ben Guerir 43150, Morocco; amina.guessabi@um6p.ma
[9] Département de Physique, Laboratoire des Revêtements, Matériaux et Environnement (LR-ME), Université de Boumerdès, Boumerdes 35000, Algeria; b.bouaouina@univ-boumerdes.dz
* Correspondence: aurelien.besnard@femto-st.fr

Abstract

This paper investigates the properties of zirconium oxide thin films deposited on Ti6Al4V and Si substrates via oblique angle deposition, using varying out-of-plane θ (15 to 85°) and in-plane Φ (0 and 180°) substrate orientations. ZrO_2 films have garnered significant interest due to their antibacterial properties and mechanical performance. The aim is to engineer surfaces capable of inhibiting bacterial growth while maintaining excellent mechanical integrity. The methodology combines experimental deposition by DC magnetron sputtering with multi-scale simulations using SRIM and SIMTRA. Structural analyses were conducted via X-ray diffraction, while microstructure and surface morphology were examined using scanning electron microscopy and atomic force microscopy. Nanoindentation tests were performed to assess hardness and elastic modulus. Results revealed that increasing the incidence angle α from 7 to 74° significantly affected surface morphology, microstructure, film thickness, and columnar tilt. The hardness and Young's modulus of the films exceeded those of Ti6Al4V, for incidence angle α between 7 and 50°, but decreased with the increasing incidence angle α. Furthermore, the films exhibited strong antibacterial activity against Gram-positive pathogens (*Staphylococcus aureus*), particularly at the highest incidence angle α, with inhibition rates exceeding 90%.

Keywords: ZrO_2 thin films; oblique angle deposition (OAD); microstructure; mechanical properties; morphology; antibacterial properties

1. Introduction

The biomedical field increasingly seeks to integrate materials science with medicine to develop innovative solutions for the repair and replacement of human tissues. Within this context, our research aims to improve the mechanical and biological performance of biomaterial alloys.

Among metallic biomaterials, cobalt-chromium alloy (CoCrMo), stainless steel 316L, and titanium alloys are the most commonly used [1]. For biomedical implants, Ti6Al4V is often preferred due to its Young's modulus (101–120 GPa) and hardness (3–4 GPa) [2]. However, in aggressive environments, the passive oxide film that forms spontaneously on its surface can degrade [3], leading to bacterial adhesion and chronic inflammation. Consequently, this native protective layer is often insufficient to guarantee optimal implant performance. Although Ti6Al4V exhibits excellent resistance to wear and corrosion, additional surface protection is required in corrosive environments.

Antibacterial adhesion is a key criterion for evaluating biomaterial suitability, as it is closely linked to the surface properties and tissue-implant interactions. Various antimicrobial materials have been investigated for their ability to gradually release antimicrobial agents to inhibit microbial growth [4]. One can cite metals like silver [5], copper [5,6], and zinc [6,7], as well as ceramics such as ZrO_2 [7–9].

Thin film deposition is one of the most conventional and effective approaches for enhancing surface bioactivity and extending implant lifespan [10]. An effective film must adhere well to the substrate and exhibit suitable mechanical properties. Zirconium is a promising candidate due to its excellent biocompatibility and acceptable mechanical behavior [11]. Zirconia-based ceramics (ZrO_2) are particularly notable among oxide ceramics for their fracture toughness and mechanical strength [12]. They exhibit low bacterial adhesion and reduced peri-implant inflammation [13], do not trigger inflammatory pathways [14], and are biocompatible without pseudo-teratogenic effects [15].

The aim of this work is to characterize and evaluate the bioactivity and potential application of OAD-deposited ZrO_2 thin films on Ti6Al4V. The thin films were deposited via DC magnetron sputtering onto Ti6Al4V and silicon substrates. The novelty of this work lies in the variation in both the out-of-plane θ (15 to 85°) and the in-plane Φ (0 and 180°) substrate angles on the substrate holder. To do so the OAD (oblique angle deposition), also known as GLAD (glancing angle deposition), technique was employed. This method involves varying the incidence angle α of the incoming atomic flux relative to the substrate normal [16]. Experimental deposition (DC magnetron sputtering) was combined with multi-scale numerical simulations using the Monte Carlo codes SRIM [17] and SIMTRA [18]. It allows us to determine the angular distribution of the particle flux, which governs the formation of inclined columnar microstructures and thereby affects the film properties. The structure was analyzed using X-ray diffraction (XRD). The microstructure and surface morphology were observed via scanning electron microscopy (SEM) and atomic force microscopy (AFM), and mechanical properties were assessed by nanoindentation. The wettability was evaluated using physiological water and ethylene glycol. Finally, antibacterial properties were assessed using standard plate count methods to determine antimicrobial activity.

2. Materials and Methods

This section outlines the experimental procedures conducted in this study, including the preparation of the substrate materials, the deposition of the films, the characterization and analytical techniques used to evaluate their physico-chemical and mechanical properties, as well as the antibacterial assays

2.1. Substrate Materials

A high-purity zirconium target (99.99 at.%, 50 mm in diameter, 6 mm thick) was used. Single-side mirror-polished (100) silicon substrates (15 × 15 × 0.38 mm) were employed for film thickness measurements, morphological observations in cross-section (column tilt angle β) and top view, chemical analysis, and structural characterization. Ti6Al4V grade 5 titanium alloy substrates (15 × 15 × 3 mm) were used for mechanical and bioactivity assessments. The Ti6Al4V substrates were polished using SiC abrasive papers ranging from 180 to 4000 grit to achieve a surface roughness Ra ≤ 0.06 µm, in accordance with ISO 7206-2:2011 [19]. All substrates were cleaned with ethanol and dried prior to deposition. They were then immediately mounted on a custom-designed substrate holder for OAD and placed into the vacuum chamber.

2.2. Film Deposition

Prior to deposition, the vacuum chamber was evacuated to a base pressure of 1×10^{-4} Pa. The working pressure was maintained at 0.24 Pa, with gas flow rates of 2 sccm for argon and 1.5 sccm for oxygen. The discharge voltage was set to −320 V with a constant current of 300 mA. The deposition time for each substrate type (Si and Ti6Al4V) was six hours. The substrates remained static throughout the deposition process.

The characteristics of the ZrO_2 flux were calculated using the SIMTRA software (v2.2), based on the experimental working pressure and system geometry. The initial angular and energy distributions were obtained using SRIM, with the experimental discharge voltage serving as the ion energy input (in eV). A total of 10^5 particles were simulated in SRIM and 10^7 in SIMTRA.

To investigate the various incidence configurations, a custom-designed substrate holder developed in a previous study [20] was employed. It consists of a base plate onto which individual holders are mounted, each with a specific out-of-plane inclination (substrate tilt angle θ) and two possible in-plane orientations (substrate orientation angle Φ). The target-to-substrate distance was fixed at 85 mm, and the center of each substrate was positioned 30 mm from the system's central axis. A schematic representation of the system geometry is shown in Figure 1.

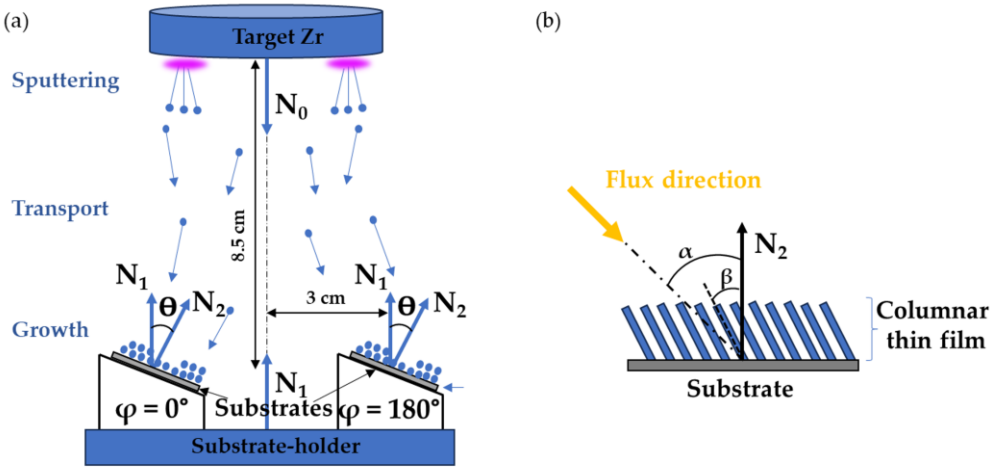

Figure 1. Principle of the OAD technique: (**a**) Schematic representation of the system geometry showing the out-of-plane substrate tilt angle θ and the in-plane substrate orientation Φ; (**b**) Illustration of the columnar structure formed within the deposited film.

N_0, N_1, and N_2 represent the normal to the target, the normal to the substrate-holder plate, and the normal to the substrate, respectively. The substrate tilt angle θ is defined as the angle between the normal to the substrate N_2 and the normal to the substrate-holder plate N_1, which is assumed to be collinear with the target normal N_0. The flux incidence

angle α is defined as the angle between the substrate normal N_2 and the direction of the incoming atomic flux (dashed line in Figure 1b). Following deposition, a thin film is formed with an inclined columnar microstructure, characterized by the column tilt angle β, defined as the angle between the substrate normal N_2 and the growth direction of the columns. While α can only be determined through simulation, β is measured from cross-sectional SEM images of the films [16].

Seven substrate tilt angles θ were available on the substrate-holder: 15, 30, 45, 60, 75, and 85°, each with two possible in-plane orientation angles Φ: 0° (facing the target) and 180° (facing the chamber wall). Using SIMTRA simulations, six [θ; Φ] configurations were selected to cover a wide range of incidence angles α, from 7° to 74° (Table 1).

Table 1. Synthesis of the flux incidence angle α as a function of substrate tilt angle θ and in-plane orientation angle Φ.

Incidence Angle α (°)	Out-of-Plane Substrate Tilt Angle θ (°)	In-Plane Substrate Orientation Angle Φ (°)
6.9	15	0
22	45	0
36.7	60	0
49.9	30	180
60.0	85	0
74.0	60	180

In the following sections, the samples will be presented according to the flux incidence angle α, along with a reminder of their corresponding geometrical configuration [θ; Φ].

2.3. Physico-Chemical and Mechanical Characterizations

This section details the experimental techniques used to characterize the morphological, physico-chemical, and mechanical properties of the deposited layers.

The elemental composition was analyzed via energy-dispersive X-ray spectroscopy (EDS X-Max N, Oxford Instruments, Abingdon-on-Thames, UK). The cross-sectional microstructure and surface morphology were observed using field emission scanning electron microscopy (FE-SEM, JSM7610F, JEOL, Tokyo, Japan).

Three-dimensional film imaging was performed by atomic force microscopy in non-contact mode (Veeco Dimension icon, Bruker, Billerica, MA, USA). Surface roughness measurements were obtained with Gwyddion.

The crystal structure of ZrO_2 thin films was examined using X-ray diffraction (XPERT-PRO, PANalytical, Malvern, UK) with a powder diffractometer operating with Cu Kα radiation (0.154 nm). Measurements were performed with a step size of 0.017° over a 2θ range of 10 to 65°, at 40 kV and 40 mA.

Nanoindentation tests were conducted on a CSM Nano Instrument (Anton Paar, Graz, Austria) using a Berkovich indenter to determine the nano-hardness and Young's modulus of the films. For each sample, the reported values represent the mean of ten series of measurement, with 25 replicates per series.

Wettability was assessed on a contact angle meter system (Dataphysics Filderstadt, Germany) by placing a 6 µL droplet of liquid (physiological water and ethylene glycol) onto the ZrO_2 surface using a syringe. Three replicates were performed for each substrate tilt angle. Contact angles were measured from images captured via a camera, and analyzed using SCA 20 software. The surface energy was calculated from the contact angle data using the Owens-Wendt-Rabel-Kaelble (OWRK) method, which modifies the Young-Dupré equation [21] to account for both polar and dispersive components of surface energy.

2.4. Antibacterial Test

The antibacterial tests were conducted to evaluate the effectiveness of the ZrO_2 OAD films in inhibiting the microbial growth. This assessment is critical in the biomedical field, as it determines the film's ability to prevent post-implant infections and ensure its biocompatibility in biological environments. The antibacterial activity of the ZrO_2 films was evaluated against the pathogenic Gram-positive bacterial strain *Staphylococcus aureus* ATCC 29213 (Figure 2).

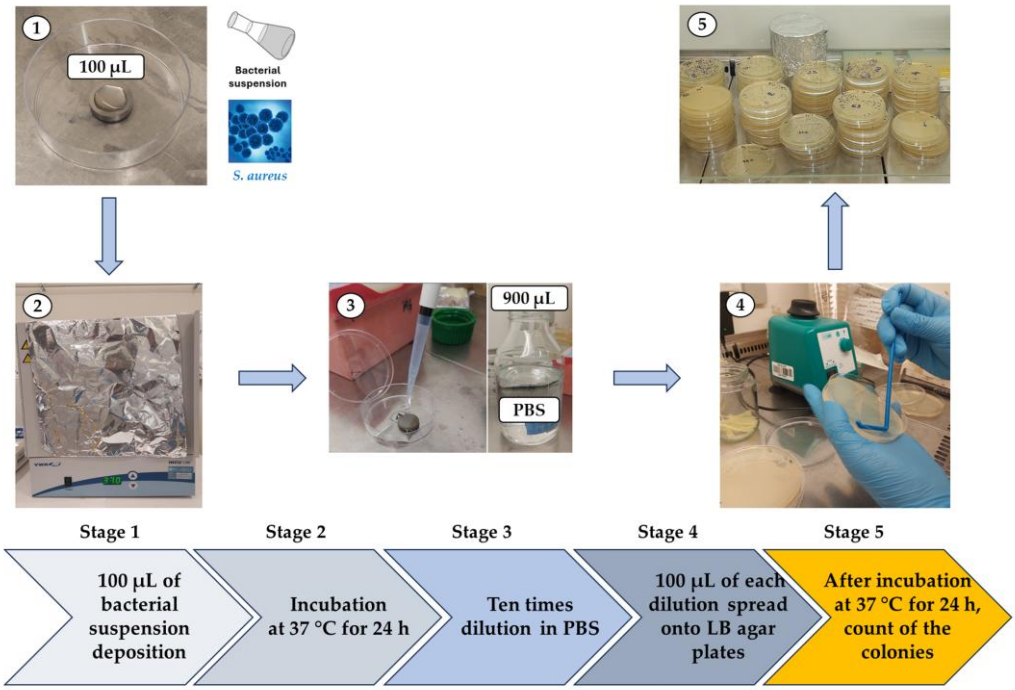

Figure 2. Schematic representation of the standard plate count method used to assess the antimicrobial activity of the samples.

The antibacterial properties of ZrO_2 thin film surfaces were further evaluated using the standard plate count method. *S. aureus* was first activated on Mueller-Hinton agar and then transferred to Luria–Bertani (LB) broth [22] to prepare the bacterial suspension. The inoculum was incubated in a shaking incubator at 120 rpm for 24 h at 37 °C. All materials were sterilized in an autoclave for 30 min at 120 °C and then aseptically transferred under a laminar flow hood into sterile Petri dishes (60 mm in diameter, 15 mm height). A volume of 100 µL of bacterial suspension was deposited onto the surface of each sample and incubated for 24 h at 37 °C.

After incubation, 900 µL of phosphate-buffered saline (PBS) was added to each sample and used to wash the surface several times. This solution served as the stock for serial dilutions, which were prepared using PBS. The control sample (uncoated Ti6Al4V) was treated identically to the coated samples. From each dilution, 100 µL was spread onto LB agar plates, which were then incubated for 24 h at 37 °C. Colony counts were performed after incubation. Each tilt angle was tested in triplicate, and the entire experiment was repeated three times.

The number of colony-forming units (CFU) was calculated using Equation (1) [23]:

$$\text{CFU} = \frac{\text{Number of colonies} \times \text{Dilution Factor}}{\text{Volume Plated (mL)}} \quad (1)$$

The dilution factors applied to the control sample and the coated substrates were 10^{-6} and 10^{-5}, respectively. The colony counts were used to evaluate the extent of bacterial inhibition on each surface.

The inhibition rate (IR), expressed as the percentage of microbial growth inhibition, was calculated using Equation (2):

$$IR = \frac{C-T}{C} \quad (2)$$

C represents the number of CFU in the control sample, while T denotes the CFU count in the treated (coated) sample.

3. Results and Discussion

This section presents and analyzes the experimental results obtained for ZrO_2 films deposited via oblique angle deposition. The microstructural and crystallographic analyses provide insights into the morphological evolution and the phase transformations induced by variations in the flux incidence angle. The nanoindentation measurements yield essential data on hardness and elastic modulus. The wettability studies reveal the influence of surface topography on interactions with biological fluids, while the antibacterial tests evaluate the films' effectiveness in preventing microbial colonization.

3.1. Chemical Composition

The chemical composition of the ZrO_2 films deposited via OAD was analyzed using EDS. The evolution of atomic oxygen concentration as a function of the incidence angle α is shown in Figure 3.

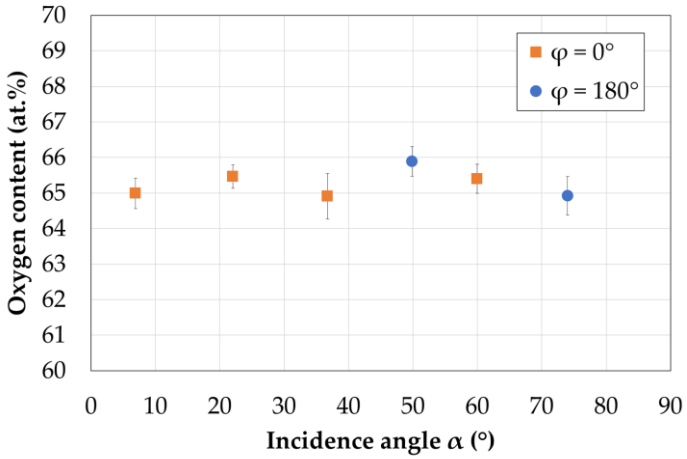

Figure 3. Atomic oxygen concentration in the ZrO_2 films as a function of the incidence angle α.

All films present a slightly under-stoichiometric oxygen content of 65.3 at.% ± 0.5. This oxygen concentration remains constant despite the increase in flux incidence angle α. This finding confirms that the reactive gas flow dominates over any potential contaminant flux (e.g., water vapor), which could increase the oxygen amount incorporated in the films for the high incidence configurations.

3.2. Microstructure

The morphological evolution of ZrO_2 films, observed in both cross-section and top view, with increasing incidence angle α is shown in Figure 4.

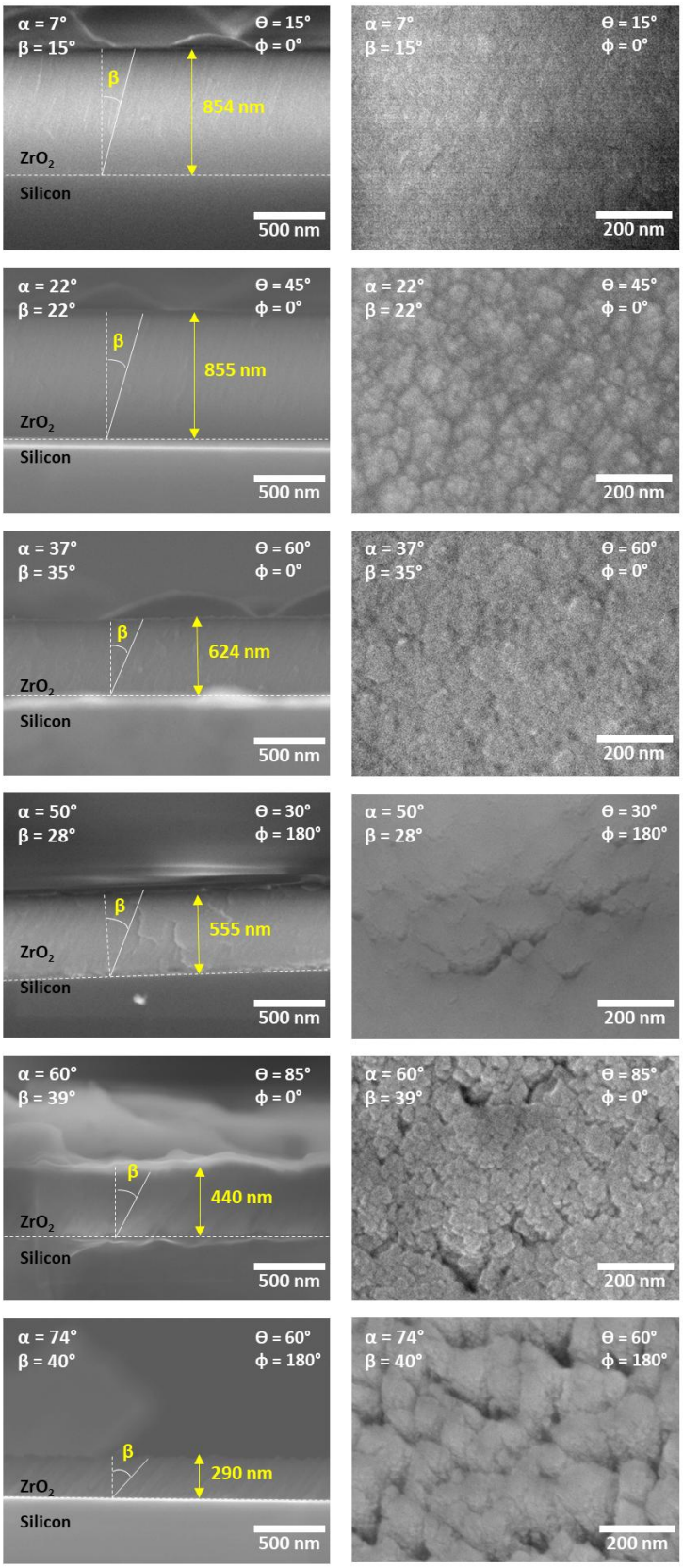

Figure 4. SEM cross-sectional (**left column**) and surface morphology (**right column**) images of ZrO_2 films deposited via oblique angle deposition (OAD) at various incidence angles α.

Cross-section observations (Figure 4 left column) reveal that all deposited films exhibit a columnar structure. An increase in the flux incidence angle α is accompanied by a reduction in film thickness and an increase in the column tilt angle β. Top-view observations (Figure 4, right column) reveal that the column tops consist of an aggregation of small nodules approximately ten nanometers in size. At low incidence angles (i.e., $\alpha < 45°$), the films appear compact and homogeneous. As the incidence angle increases (i.e., $\alpha > 45°$), the surface morphology evolves, exhibiting more pronounced open porosity in the form of rifts oriented perpendicular to the flux direction. The density of these voids increases with α, indicating a significant rise in porosity beyond 45°, especially for the highest incidence angle $\alpha = 74°$. This increase in porosity with incidence angle has been previously reported by Rahmouni et al. [20], Wada et al. [24], and Sobahan et al. [25], and is attributed to the shadowing effect [26]. Similar morphological trends have been observed in other oxide films deposited via OAD, including Ta_2O_5 [25], Nb_2O_5 [27], ZnO [28], and TiO_2 [29]. The increase in porosity with incidence angle is associated with an increase in the roughness. AFM measurements show that the Ra slightly increased for $\alpha < 60$ with an average value of 36 nm ± 5, and suddenly increased to Ra = 61 nm ± 12 for $\alpha = 74°$.

From the SEM cross-sectional images (Figure 4, left column), both the film thickness t and the column tilt angle β were measured. The evolution of these two parameters as a function of the incidence angle α is presented in Figure 5.

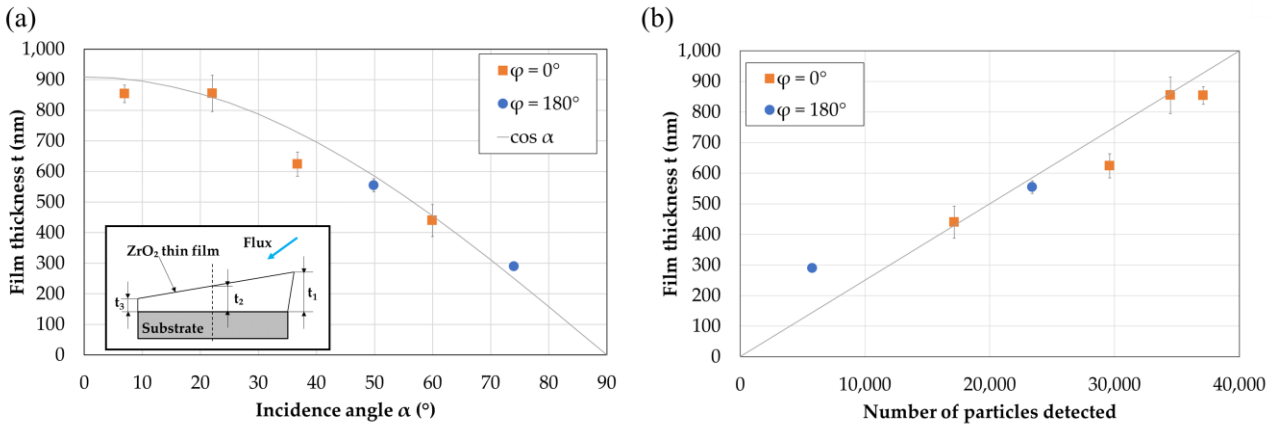

Figure 5. (**a**) Experimental ZrO_2 film thickness t as a function of the incidence angle α; (**b**) Number of particles obtained from SIMTRA simulations plotted against the experimentally measured film thickness; (a-inset) Thickness variation between the edges and the center of an OAD thin film.

As films deposited on inclined substrates exhibit a thickness gradient, the average thickness of each film was measured from three distinct positions (i.e., top, middle, and bottom of the substrate; t_1, t_2, and t_3, respectively) relative to the flux direction (Figure 5a, inset). As observed in the SEM images presented in Figure 4, the thickness of ZrO_2 films decreases from 850 to 290 nm as the incidence angle α increases. From a geometrical standpoint, the amount of vapor flux striking a flat substrate is proportional to the projected surface area of the inclined substrate in a plane parallel to the target. Consequently, the film thickness t will follow the cosine of the incidence angle α and can be calculated using Equation (3):

$$t = t_0 . \cos \alpha \quad (3)$$

where t_0 is the film thickness under normal incidence conditions ($\alpha = 0°$), and α is the incidence angle. This relation is confirmed for the ZrO_2 films as presented in Figure 5a.

Figure 5b shows the relationship between the experimentally measured thickness of ZrO_2 films and the number of particles obtained from SIMTRA simulations. A strong linear

correlation is observed between the experimental data and the SIMTRA simulations, indicating that the simulation accurately reproduces the experimental behavior. This confirms a positive correlation between the amount of deposited material (represented by detected particles) and the measured film thickness.

Figure 6 illustrates the evolution of the column tilt angle β of ZrO_2 films as a function of the incidence angle α. The two most commonly referenced theoretical models are presented for comparison: Tait's rule [30] and the tangent rule [31] (Equations (4) and (5), respectively).

$$\beta=\alpha\text{-}\arcsin\left(\frac{1-\cos\alpha}{2}\right) \quad (4)$$

$$\tan\beta=\frac{1}{2}\tan\alpha \quad (5)$$

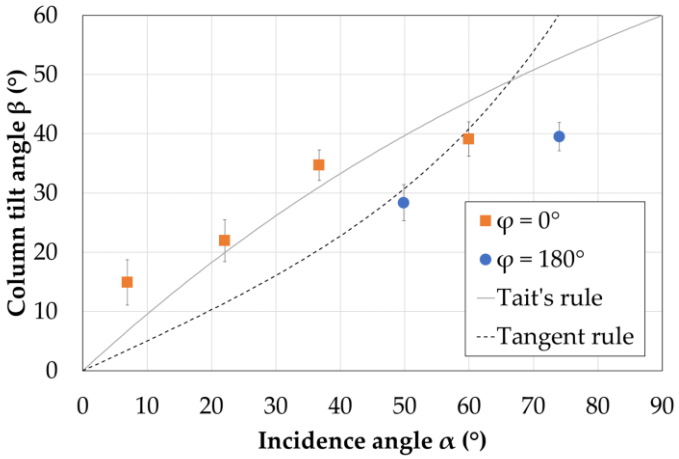

Figure 6. Column tilt angle β as a function of the incidence angle α.

The column tilt angle β increases progressively from 15 to 40° as the flux incidence angle α increases from 7 to 74°, following a trend similar to that predicted by Tait's rule. For $\alpha < 45°$, the measured column tilt angle β slightly exceeds the value predicted by Tait's rule, whereas for $\alpha > 45°$, β remains below the theoretical prediction. Although the incidence angle α calculated via simulation is the most accurate descriptor of the incoming flux [16] (the substrate tilt angle θ serves only as a geometrical parameter of the substrate holder), the growth direction, and thus the column tilt angle β, is also influenced by the angular and energy distributions of the atomic fluxes (metal and reactive gas) and by the oxide formation. Due to scattering effects during transport and the geometrical configuration (θ and Φ), the proportion of the flux arriving at low incidence angles increases relative to that arriving at high angles as the incidence angle α increases. This shift contributes to the observed deviation from theoretical models and affects the final columnar structure of the films.

3.3. Structure

Figure 7 shows the XRD patterns of ZrO_2 thin films deposited on silicon substrates at increasing incidence angles α.

The main diffraction peaks observed at 29.5, 33.6, 38.6, 39.5, 43.3, 44.8, 47.6, 48.6, and 61.8° are attributed to the (−111), (200), (021), (210), (121), (112), (212), (−212), and (−133) planes, as indexed in the JCPDS card No. 00-037-1484 [32] for the monoclinic phase of ZrO_2. Some peaks appear slightly shifted compared to the reference positions of the monoclinic

phase. According to Bragg's law ($2 \cdot d \cdot \sin(\theta) = n \cdot \lambda$, where n and λ are constants), such shifts may indicate the presence of compressive or tensile stresses within the film [33].

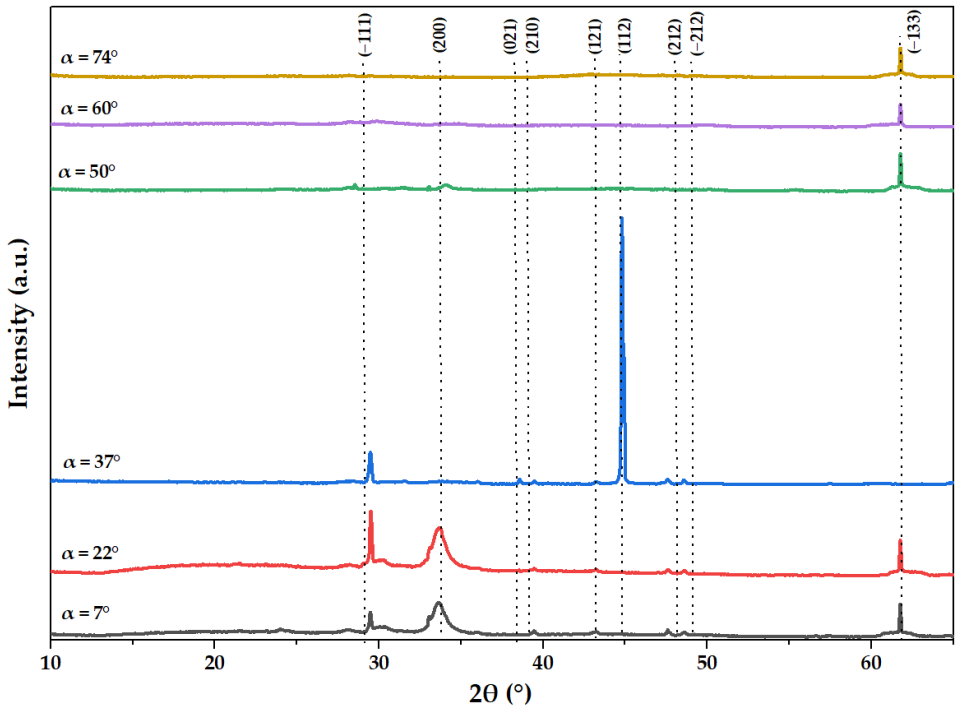

Figure 7. XRD patterns of the ZrO_2 films at various incidence angles α.

At incidence angles α = 7 and 22°, the main diffraction peak corresponds to the (200) plane. At α = 37°, a sudden change is observed, with a strong peak emerging for the (112) plane. For incidence angles above 45°, the diffraction patterns exhibit attenuated intensities, except for the (−133) plane. One possible explanation is the amorphization of the films, induced by an increased thermalized fraction of the vapor flux, which reduces adatom mobility [34]. However, as the columnar structure tilts progressively with increasing incidence angle α, a corresponding tilt of the crystallites within the columns is also expected [35]. It can be assumed that at α = 7 and 22°, the crystallite tilt remains minimal, maintaining the (200) orientation. At α = 37°, the crystallites undergo a sudden reorientation, allowing the (112) plane to satisfy the diffraction condition. For higher incidence angles, the crystallites continue to tilt in the direction of the vapor flux, resulting in no planes being favorably oriented for diffraction, thereby producing an amorphous-like pattern.

3.4. Mechanical Properties

To investigate the effect of the incidence angle on film hardness and Young's modulus, the evolution of these two parameters with increasing incidence angle α is presented in Figure 8.

The Young's modulus (E) and nanohardness (H) of the ZrO_2 films decrease with increasing incidence angle α. Hardness shows a continuous decline from 8.35 to 1.62 GPa, while the Young's modulus remains nearly constant at approximately 195 ± 43 GPa before dropping to 96 ± 19 GPa at the highest incidence angle. At low incidence angles, these values are consistent with those reported in the literature for bulk ZrO_2 and thin films deposited under conventional deposition configurations, where hardness is typically around 9.2 GPa and Young's modulus ranges between 150 and 200 GPa [36]. At higher incidence angles, similar trends have been observed for chromium thin films deposited via the OAD method

by Lintymer et al. [37]. They reported a decrease in hardness from 5.25 to 1.8 GPa and in Young's modulus from 172 to 85 GPa as the incidence angle increased from 0 to 50°. For comparison, the titanium alloy Ti6Al4V, used as substrate, exhibits a Young's modulus between 101 and 120 GPa and a hardness of 3–4 GPa [2]. Except for the two highest incidence angles, the ZrO_2 films deposited using the OAD technique and varying incidence angles between 7 and 50° demonstrate higher mechanical properties than the substrate.

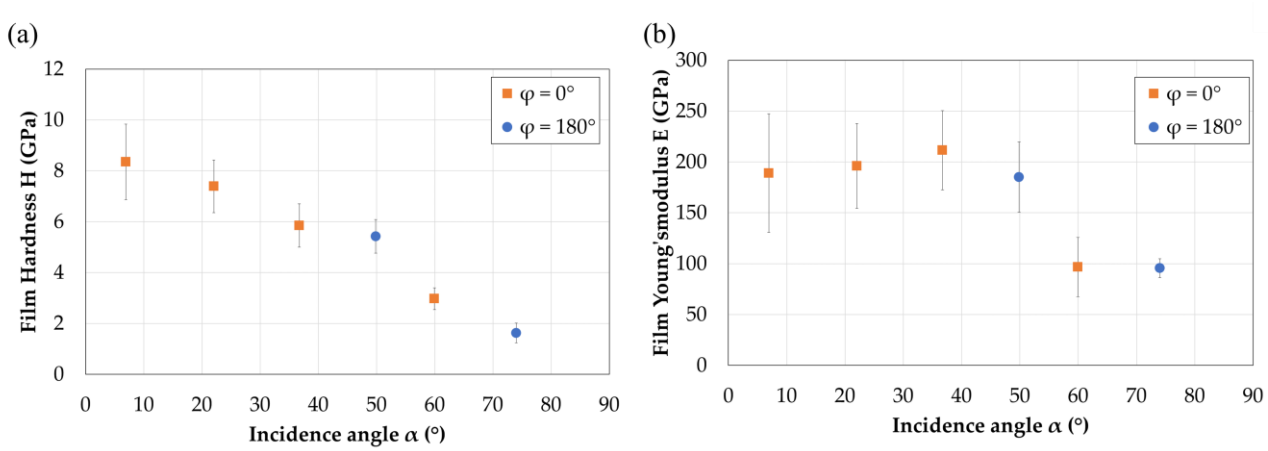

Figure 8. Hardness H (**a**) and Young's modulus E (**b**) of ZrO_2 films as a function of the incidence angle α.

The continuous decrease in hardness is primarily attributed to the increase in incidence angle α. This leads to an increase in the column tilt angle β and an enhanced intercolumnar porosity due to the shadowing effect. As shown in the SEM top-view images (Figure 4) and column tilt angle analysis (Figure 6), open porosity becomes more pronounced with increasing α, especially for $\alpha \geq 45°$, where the shadowing effect is more significant [38]. Hardness, which reflects resistance to plastic deformation, is mainly influenced by variations in overall film density and morphology [37]. In contrast, Young's modulus, as an intrinsic material property, remains relatively unaffected until microstructural changes become dominant. For a constant Young's modulus, a column tilt angle β near 45°, potentially coupled with crystallite tilt and significant porosity, results in reduced film stiffness.

Previous studies on tribological applications have shown that mechanical durability and resistance to failure in films are enhanced by combining high hardness with a low elastic modulus [39]. In this context, a high H/E ratio, which reflects resistance to elastic strain before failure, is considered beneficial. It indicates the material's ability to undergo elastic deformation and redistribute applied loads over a larger area, thereby delaying failure. Similarly, a high H^3/E^2 ratio, indicative of resistance to plastic deformation, is also crucial [40], with optimal values typically ranging from 0.15 to 0.3 [41]. However, these criteria only provide a tendency of the film behavior and do not directly predict the resistance in the service of the system.

Various studies have shown that films with an H/E ratio ≥ 0.1 exhibit high resistance to plastic deformation and low elastic strain to failure, whereas those with H/E ≤ 0.1 tend to be more brittle and less elastic [42]. As shown in Figure 9a, the H/E ratio of the ZrO_2 films gradually decreases with increasing flux incidence angle α. The ZrO_2 thin films deposited via the OAD technique exhibit H/E values below 0.1, ranging from 0.045 to 0.015, indicating limited elastic strain before failure. These low values suggest that the films are prone to cracking due to their limited elasticity. The H^3/E^2 ratios presented in Figure 9b follow similar trends to H/E, with low values ranging from 0.016 to 0.001, indicating poor resistance to plastic deformation. Although ZrO_2 films show good hardness and Young's modulus

values, their low H/E and H^3/E^2 ratios suggest that the films are relatively brittle and have limited deformation capacity.

Figure 9 illustrates the evolution of these two parameters as a function of the incidence angle α.

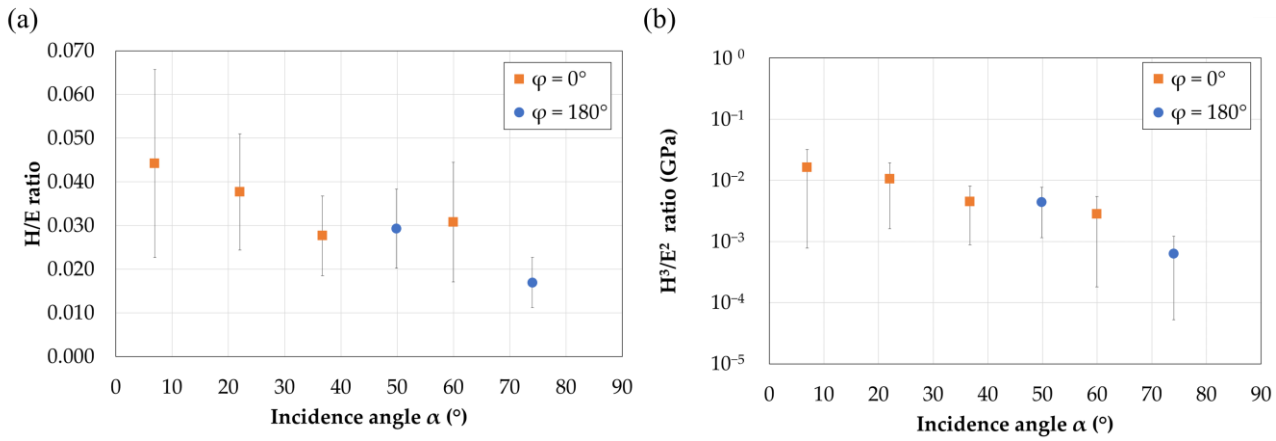

Figure 9. Resistance to elastic deformation H/E (**a**) and plastic deformation H^3/E^2 (**b**) of ZrO_2 films as a function of the incidence angle α.

Nevertheless, these values are not critical, as they are similar to those of bulk monoclinic zirconia. To improve these mechanical indicators, doping strategies such as yttrium incorporation should be considered. According to Wei et al. [43], the cellular structure of the tetragonal phase plays a key role in the toughness of YSZ-based ceramics. The reported values for YSZ are H/E = 0.05 and H^3/E^2 = 0.015, slightly higher than those of the OAD ZrO_2 films.

3.5. Wettability

The wettability is influenced by both surface energy and topography. According to Young's equation [44], materials with higher surface energy tend to exhibit lower water contact angles. Evaluating wettability is essential for understanding the bacterial adhesion behavior. Indeed, numerous studies have shown that bacteria preferentially adhere to surfaces with moderate wettability [45]. Han et al. [11] reported that hydrophobic surfaces are more effective in preventing bacterial adhesion.

The contact angle of ZrO_2 films was measured using two liquids: physiological water and ethylene glycol. The variation in the contact angle with respect to the incidence angle α is presented in Figure 10.

For both physiological water and ethylene glycol, the ZrO_2 films exhibit neither distinctly hydrophobic nor hydrophilic behavior at incidence angles α below 45°, with contact angles around 90°. The films are slightly hydrophobic when tested with physiological water and slightly hydrophilic with ethylene glycol. At incidence angles α above 45°, corresponding to more inclined columns and increased surface roughness, the films become hydrophobic for both liquids, and the contact angle increases with α. Overall, the contact angles measured for the two liquids are relatively similar. The main factors influencing the contact angle of liquid droplets on a solid surface are the chemical composition and the surface roughness, both of which are closely linked to the material's microstructure [46]. Patel et al. [47] reported similar contact angle values with water and attributed the variations to changes in surface roughness.

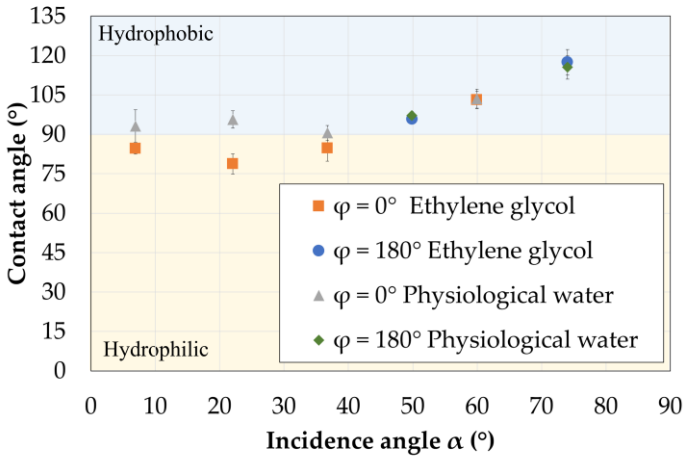

Figure 10. Contact angle of ZrO_2 films as a function of the incidence angle α, measured with physiological water and ethylene glycol.

The surface energy of ZrO_2 films was calculated from the contact angle measurements using the Owens-Wendt model [21], and is presented in Figure 11.

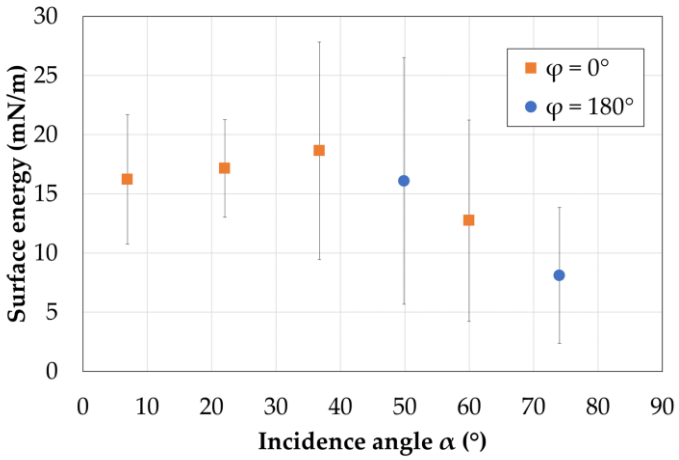

Figure 11. Variation in the surface energy of ZrO_2 films as a function of the incidence angle α.

For incidence angles α below 45°, the average surface energy of ZrO_2 films is approximately 17 ± 6 mN/m, and progressively decreases to 8 ± 5 mN/m as α further increases. According to Hao and Lawrence [48], surface wettability is a key factor in cell adhesion, as it is directly related to the surface energy and is typically assessed via contact angle measurements. In general, higher surface free energy enhances the cell adhesion and improves biocompatibility. Surface roughness, surface energy, and material composition are the three primary factors influencing bacterial adhesion. A surface roughness threshold of 0.2 µm has been identified, above which bacterial adhesion tends to increase [49]. This value is higher than the Ti6Al4V substrates' roughness ($Ra \leq 0.06$ µm) and the film roughness ($Ra < 62$ nm).

Regarding surface energy, low-energy surfaces in the range of 20–30 mN/m, as observed for the ZrO_2 films in this study, have been shown to minimize bacterial adhesion [50]. Based on these considerations, the antibacterial behavior of the ZrO_2 films appears promising.

3.6. Antibacterial Behavior

S. aureus strains are known to frequently cause severe implant-related infections [51]. To evaluate the antimicrobial efficacy of the coated substrates against *S. aureus*, the

inhibition rate was determined for all ZrO_2 films deposited at various incidence angles, as shown in Figure 12.

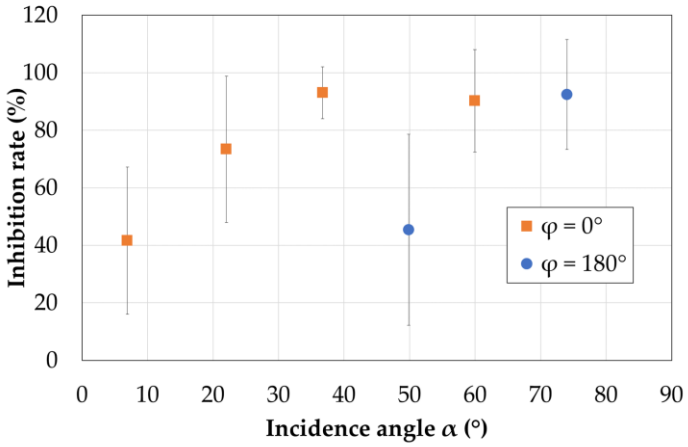

Figure 12. Inhibition of *S. aureus* growth by ZrO_2 films as a function of the incidence angle α.

As shown in Figure 12, compared to the uncoated reference sample, significant bacterial inhibition against *S. aureus* was observed. A very low number of bacteria was observed, indicating that the ZrO_2 films exhibit excellent in vitro antibacterial activity. The absence of bacterial growth on culture plates suggests a bactericidal effect of the samples.

Except for the sample deposited at $\alpha = 50°$, the inhibition rate of *S. aureus* increased from 40 to 95%, correlating with the incidence angle α. These results are consistent with the trends in wettability and surface energy discussed previously (Figures 10 and 11). This behavior may be attributed to the increased surface roughness and the structural characteristics of the ZrO_2 thin films, including the tilt of crystallites within the columns, which may hinder bacterial penetration and enhance antibacterial performance. In addition, the electrostatic interaction between the positively charged surface of ZrO_2 and the negatively charged bacterial membrane can lead to bacterial membrane destruction and leakage of cellular content (ions, proteins, and nucleic acids), resulting in cell death or high growth inhibition [52,53]. The anomalous behavior observed at $\alpha = 50°$ may be due to variability in the initial bacterial suspension or during the incubation process.

According to Abdulrazaq et al. [8], co-culture is the most effective method for evaluating the antibacterial properties of nanocomposites. They reported that pure ZrO_2 exhibited 98.8% inhibition against *S. aureus*, and no bacterial growth was observed with Polyvinylpyrrolidone-ZrO_2 nanocomposites against Gram-positive pathogenic bacteria compared to the control.

The antibacterial efficiency of PVD-deposited ZrO_2 films on Ti6Al4V substrates is highly dependent on the specific surface characteristics, which are influenced by the chemical nature of the material and controlled by the incidence angle α. This highlights the critical role of deposition geometry in determining the functional performance of thin films.

Future studies could explore strategies to enhance the bioactivity of ZrO_2 films at various inclination angles, such as the addition of a Zn layer on top of the ZrO_2 films. As demonstrated by Wang et al. [52], Zn–ZrO_2/TiO_2 films exhibit excellent antibacterial properties and hold promise for applications in titanium alloy implants. This enhanced antibacterial activity is primarily attributed to the release of Zn^{2+} ions, which effectively suppress bacterial growth.

4. Conclusions

In this study, the oblique angle deposition (OAD) technique was employed to synthesize zirconium oxide (ZrO_2) thin films with varying substrate orientations defined by out-

of-plane θ and in-plane Φ angles, resulting in variable flux incidence angles α. The main findings of this work can be summarized as follows:

- The microstructural evolution of the films follows expected trends with increasing flux incidence angle: a cosine-dependent decrease in film thickness (from 850 to 290 nm), an increase in column tilt angle consistent with Tait's rule (from 14.9 to 39.5°), and morphological changes, including increased surface roughness and intercolumnar porosity.
- X-ray diffraction (XRD) analysis confirms the presence of the monoclinic phase of ZrO_2, as expected in the absence of dopants such as yttria (used to stabilize the ZrO_2 tetragonal and cubic phases). Apparent amorphization is observed with increasing column tilt, which may also result from texture effects due to crystallite and column orientation.
- Mechanical characterization shows that ZrO_2 films possess good hardness and Young's modulus values. However, due to the inclined columnar microstructure and associated porosity, the films exhibit limited resistance to plastic and elastic deformation.
- Bioactivity against *Staphylococcus aureus* is excellent, with inhibition rates exceeding 90% at high incidence angles. This is attributed to increased surface roughness and microstructural features that hinder bacterial colonization.

Author Contributions: Conceptualization, A.G. (Asma Gzaiel) and A.B.; methodology, A.B.; investigation, A.G. (Asma Gzaiel), K.A., A.B., Y.P., Y.A.B.S., A.G. (Amina Guessabi), and B.B.; resources, F.B.; writing—original draft preparation, A.G. (Asma Gzaiel); writing—review and editing, A.G. (Amina Guessabi), K.A., A.B., Y.P., C.N., F.B.; supervision, K.A., A.B., C.N., F.B.; All authors have read and agreed to the published version of the manuscript.

Funding: This research was funded by the Ministry of Higher Education and Scientific Research of Tunisia and by UM6P (Morocco) with a two-month internship and financial support.

Data Availability Statement: The data presented in this study are available on request from the corresponding author.

Acknowledgments: The authors acknowledge Anouar Ounis for his assistance with the XRD measurements at Tunis El Manar University, Romaric Masset and Denis Lagadrillère for their help during the experiments at LaBoMaP, and Tamim Bounnite for his support with the wettability tests at UM6P.

Conflicts of Interest: The authors declare no conflicts of interest.

References

1. Bekmurzayeva, A.; Duncanson, W.J.; Azevedo, H.S.; Kanayeva, D. Surface modification of stainless steel for biomedical applications: Revisiting a century-old material. *Mater. Sci. Eng. C* **2018**, *93*, 1073–1089. https://doi.org/10.1016/j.msec.2018.08.049.
2. Aniołek, K.; Kupka, M. Surface characterization of thermally oxidized Ti-6Al-7Nb alloy. *Mater. Chem. Phys.* **2016**, *171*, 374–378. https://doi.org/10.1016/j.matchemphys.2016.01.031.
3. Maestro, C.A.R.; Moreto, J.A.; Chiaramonte, T.; Gelamo, R.V.; de Oliveira, C.J.F.; Santos, M.M.; da Silva, M.V.; Bueno, A.H.S.; Balestra, R.M.; de Sousa Malafaia, A.M. Corrosion behavior and biological responses of a double coating formed on the Ti6Al-4V alloy surface by using thermal oxidation and biomimetic deposition of bismuth-doped CaP. *Surf. Coat. Technol.* **2021**, *425*, 127717. https://doi.org/10.1016/j.surfcoat.2021.127717.
4. Kourani, K.; Anju, T.R.; Chirayil, C.J.; Krishnakumar, A. Strategic defenses: A review of novel approaches to combat nosocomial infections on medical implants, International. *J. Pharm.* **2025**, *681*, 125827. https://doi.org/10.1016/j.ijpharm.2025.125827.
5. Ye, L.; He, X.; Obeng, E.; Wang, D.; Zheng, D.; Shen, T.; Shen, J.; Hu, R.; Deng, H. The CuO and AgO Co-modified ZnO Nanocomposites for Promoting Wound Healing in Staphylococcus aureus Infection. *Mater. Today Bio* **2023**, *18*, 100552. https://doi.org/10.1016/j.mtbio.2023.100552.

6. Kumar, P.; Ramesh, M.R.; Doddamani, M.; Suresh, J.; Lingaraj, R. Green synthesis of CuO/MgO/ZnO nanoparticles using Costus pictus leaf extract for effective antibacterial applications. *Mater. Lett.* **2024**, *359*, 135918. https://doi.org/10.1016/j.matlet.2024.135918.
7. Abebe, B.; Zereffa, E.A.; Tadesse, A.; Murthy, H.C.A. A Review on Enhancing the Antibacterial Activity of ZnO: Mechanisms and Microscopic Investigation. *Nanoscale Res. Lett.* **2020**, *15*, 190. https://doi.org/10.1186/s11671-020-03418-6.
8. Abdulrazaq, R.A.; Al-Ramadhan, Z.A.; Khalaf, H.H. Antibacterial activity of (PVP-ZrO_2) nanocomposite against pathogenic bacteria. *World News Nat. Sci.* **2018**, *18*, 187–194.
9. Khlifi, K.; Atallah, M.S.; Cherif, I.; Karkouch, I.; Barhoumi, N.; Essaies, S.A. Synthesis of ZnO nanoparticles and study of their influence on the mechanical properties and antibacterial activity of PMMA/ZnO composite for orthotic devices. *Surface Interfaces* **2023**, *41*, 103279. https://doi.org/10.1016/j.surfin.2023.103279.
10. Su, Y.; Cockerill, I.; Zheng, Y.; Tang, L.; Qin, Y.X.; Zhu, D. Biofunctionalization of metallic implants by calcium phosphate coatings. *Bioact. Mater.* **2019**, *4*, 196–206. https://doi.org/10.1016/j.bioactmat.2019.05.001.
11. Han, J.; Zhang, F.; Meerbeek, B.V.; Vleugels, J.; Braem, A.; Castagne, S. Laser surface texturing of zirconia-based ceramics for dental applications: A review. *Mater. Sci. Eng. C* **2021**, *123*, 112034. https://doi.org/10.1016/j.msec.2021.112034.
12. Wei, C.; Gremillard, L. Towards the prediction of hydrothermal ageing of 3Y-TZP bioceramics from processing parameters. *Acta Mater.* **2018**, *144*, 245–256. https://doi.org/10.1016/j.actamat.2017.10.061.
13. Sanz-Martín, I.; Sanz-Sanchez, I.; Carrillo De Albornoz, A.; Figuero, E.; Sanz, M. Effects of modified abutment characteristics on peri-implant soft tissue health: A systematic review and meta-analysis. *Clin. Oral Implant. Res.* **2018**, *29*, 118–129. https://doi.org/10.1111/clr.13097.
14. Kunrath, M.F.; Gupta, S.; Lorusso, F.; Scarano, A.; Noumbissi, S. Oral Tissue Interactions and Cellular Response to Zirconia Implant-Prosthetic Components: A Critical Review. *Materials* **2021**, *14*, 2825. https://doi.org/10.3390/ma14112825.
15. Depprich, R.; Zipprich, H.; Ommerborn, M.; Naujoks, C.; Wiesmann, H.P.; Kiattavorncharoen, S.; Lauer, H.C.; Meyer, U.; Kübler, N.R.; Handschel, J. Osseointegration of zirconia implants compared with titanium: An in vivo study. *Head Face Med.* **2008**, *4*, 30. Available online: http://www.head-face-med.com/content/4/1/30 (accessed on 4 January 2024).
16. Besnard, A.; Gerami, H.; Raschetti, M.; Martin, N. Resultant Incidence Angle: A Unique Criterion for Controlling the Inclined Columnar Nanostructure of Metallic Films. *Nanomaterials* **2025**, *15*, 620. https://doi.org/10.3390/nano15080620.
17. Ziegler, J.F.; Ziegler, M.D.; Biersack, J.P. SRIM—The stopping and range of ions in matter. *Nucl. Instrum. Methods Phys. Res. B* **2010**, *268*, 1818–1823. https://doi.org/10.1016/j.nimb.2010.02.091.
18. Aeken, K.V.; Mahieu, S.; Depla, D. The metal flux from a rotating cylindrical magnetron: A Monte Carlo simulation. *J. Phys. Appl. Phys.* **2008**, *41*, 205307. https://doi.org/10.1088/0022-3727/41/20/205307.
19. *ISO 7206-2:2011*; Implants for surgery—Partial and total hip joint prostheses—Part 2: Articulating surfaces made of metallic, ceramic and plastics materials. International Organization for Standardization (ISO): Geneva, Switzerland, 2021; Volume 2021, p. 3.
20. Rahmouni, K.; Besnard, A.; Oulmi, K.; Nouveau, C.; Hidoussi, A.; Aissani, L.; Zaabat, M. In vitro corrosion response of CoCrMo and Ti-6Al-4V orthopedic implants with Zr columnar thin films. *Surf. Coat. Technol.* **2022**, *436*, 128310. https://doi.org/10.1016/j.surfcoat.2022.128310.
21. Ismail, M.F.; Khorshidi, B.; Sadrzadeh, M. New insights into the impact of nanoscale surface heterogeneity on the wettability of polymeric membranes. *J. Membr. Sci.* **2019**, *590*, 117270. https://doi.org/10.1016/j.memsci.2019.117270.
22. Yamamoto, K.; Toya, S.; Sabidi, S.; Hoshiko, Y.; Maeda, T. Diluted Luria-Bertani Medium vs. Sewage Sludge as Growth Media: Comparison of Community Structure and Diversity in the Culturable Bacteria. *Appl. Microbiol. Biotechnol.* **2021**, *105*, 3787–3798. https://doi.org/10.1007/s00253-021-11248-4.
23. Peng, M.; Chuan, J.L.; Zhao, G.P.; Fu, Q. Construction of silver-coated high translucent zirconia implanting abutment material and its property of antibacterial, Artificial Cells. *Nanomed. Biotechnol.* **2023**, *51*, 441–452. https://doi.org/10.1080/21691401.2023.2244013.
24. Wada, K.; Yoshiya, M.; Yamaguchi, N.; Matsubara, H. Texture and microstructure of ZrO_2-4mol% Y_2O_3 layers obliquely deposited by EB-PVD. *Surf. Coat. Technol.* **2006**, *200*, 2725–2730. https://doi.org/10.1016/j.surfcoat.2005.02.121.
25. Sobahan, K.M.A.; Park, Y.J.; Hwangbo, C.K. Effect of Deposition Angle on the Optical and the Structural Properties of Ta_2O_5 Thin Films Fabricated by Using Glancing Angle Deposition. *Korean Phys. Soc.* **2009**, *55*, 1272–1277. https://doi.org/10.3938/jkps.55.1272.
26. Potin, V.; Boukhalfa, H.; Martin, N. Oblique angle co-deposition of nanocolumnar tungsten thin films with two W sources: Effect of pressure and target current. *Mater. Chem. Phys.* **2022**, *281*, 125864. https://doi.org/10.1016/j.matchemphys.2022.125864.
27. Xiao, X.; Dong, G.; Xu, C.; He, H.; Qi, H.; Fan, Z.; Shao, J. Structure and optical properties of Nb_2O_5 sculptured thin films by glancing angle deposition. *Appl. Surf. Sci.* **2008**, *255*, 2192–2195. https://doi.org/10.1016/j.apsusc.2008.07.071.

28. Park, Y.J.; Sobahan, K.M.A.; Nam, H.J.; Kim, J.J.; Hwangbo, C.K. Optical and Structural Properties of ZnO Thin Films Fabricated by Using Oblique Angle Deposition. *Korean Phys. Soc.* **2010**, *57*, 1657–1660. https://doi.org/10.3938/jkps.57.1657.
29. Wang, S.; Xia, G.; He, H.; Yi, K.; Shao, J.; Fan, Z. Structural and optical properties of nanostructured TiO_2 thin films fabricated by glancing angle deposition. *J. Alloys Comp.* **2007**, *431*, 287–291. https://doi.org/10.1016/j.jallcom.2006.05.091.
30. Tait, R.N.; Smy, T.; Brett, M.J. Modelling and characterization of columnar growth in evaporated films. *Thin Solid Film.* **1993**, *226*, 196–201. https://doi.org/10.1016/0040-6090(93)90378-3.
31. Nieuwenhuizen, J.M.; Haanstra, H.B. Microfractography of thin films. *Philips Tech. Rev.* **1966**, *27*, 597.
32. Ahire, S.A.; Bachhav, A.A.; Jagdale, B.S.; Patil, A.V.; Koli, P.B.; Pawar, T.B. Amalgamation of ZrO_2-PANI Nanocomposite Polymeric Material: Characterization and Expeditious Photocatalytic Performance Towards Carbol Fuchsin (CF) Dye and Kinetic Study. *J. Inorg. Organomet. Polym. Mater.* **2023**, *33*, 1357–1368. https://doi.org/10.1007/s10904-023-02590-3.
33. Yousaf, M.; Pelenovich, V.; Yang, B.; Liu, C.S.; Fu, D.J. Effect of Bilayer Period on Structural and Mechanical Properties of Nanocomposite TiAlN/MoN Multilayer Films Synthesized by Cathodic Arc Ion-Plating. *Surf. Coat. Technol.* **2015**, *282*, 94–102. https://doi.org/10.1016/j.surfcoat.2015.10.018.
34. Chargui, A.; El Beainou, R.; Mosset, A.; Euphrasie, S.; Potin, V.; Vairac, P.; Martin, N. Influence of thickness and sputtering pressure on electrical resistivity and elastic wave Propagation in oriented columnar tungsten thin films. *Nanomaterials* **2020**, *10*, 81. https://doi.org/10.3390/nano10010081.
35. Abadias, G.; Angay, F.; Mareus, R.; Mastail, C. Texture and Stress Evolution in HfN Films Sputter-Deposited at Oblique Angles. *Coatings* **2019**, *9*, 712. https://doi.org/10.3390/coatings9110712.
36. Bernard, O.; Huntz, A.M.; Andrieux, M.; Seiler, W.; Ji, V.; Poissonnet, S. Synthesis, structure, microstructure and mechanical characteristics of MOCVD deposited zirconia films. *Appl. Surf. Sci.* **2007**, *253*, 4626–4640. https://doi.org/10.1016/j.apsusc.2006.10.025.
37. Lintymer, J.; Gavoille, J.; Martin, N.; Takadoum, J. Glancing angle deposition to modify microstructure and properties of sputter deposited chromium thin films. *Surf. Coat. Technol.* **2003**, *174–175*, 316–323. https://doi.org/10.1016/S0257-8972(03)00413-4.
38. Tait, R.N.; Smy, T.; Brett, M.J. Structural anisotropy in oblique incidence thin metal films. *J. Vac. Sci. Technol.* **1992**, *10*, 1518–1521. https://doi.org/10.1116/1.578037.
39. Matthews, A.; Franklin, S.; Holmberg, K. Tribological coatings: Contact mechanisms and selection. *J. Phys. D: Appl. Phys.* **2007**, *40*, 5463–5475. https://doi.org/10.1088/0022-3727/40/18/S07.
40. Musil, J.; Jirout, M. Toughness of hard nanostructured ceramic thin films. *Surf. Coat. Technol.* **2007**, *201*, 5148–5152. https://doi.org/10.1016/j.surfcoat.2006.07.020.
41. Musil, J.; Novák, P.; Čerstvý, R.; Soukup, Z. Tribological and mechanical properties of nanocrystalline-TiC/a-C nanocomposite thin films. *J. Vac. Sci. Technol.* **2010**, *28*, 244–249. https://doi.org/10.1116/1.3294717.
42. Musil, J. Hard nanocomposite coatings: Thermal stability, oxidation resistance and toughness. *Surf. Coat. Technol.* **2012**, *207*, 50–65. https://doi.org/10.1016/j.surfcoat.2012.05.073.
43. Wei, X.; Yu, Q.; Yuan, P.; Jin, P.; Li, J.; Zhu, Q.; Sun, C. Influence of TiO_2 doping and spraying power on the microstructure, mechanical properties and cavitation erosion resistance of YSZ coatings. *Ceram. Int.* **2024**, *50*, 29244–29255. https://doi.org/10.1016/j.ceramint.2024.05.220.
44. Young, T. III. An essay on the cohesion of fluids. *Philos Trans. R. Soc. Lond.* **1805**, *95*, 65–87. https://doi.org/10.1098/rstl.1805.0005.
45. Arima, Y.; Iwata, H. Effect of wettability and surface functional groups on protein adsorption and cell adhesion using well-defined mixed self-assembled monolayers. *Biomaterials* **2007**, *28*, 3074–3082. https://doi.org/10.1016/j.Biomaterials.2007.03.013.
46. Blossey, R. Self-cleaning surfaces—Virtual realities. *Nat. Mater.* **2003**, *2*, 301–306. https://doi.org/10.1038/nmat856.
47. Patel, U.S.; Patela, K.H.; Chauhana, K.V.; Chawlab, A.K.; Rawal, S.K. Investigation of various properties for zirconium oxide films synthesized by sputtering. *Procedia Technol.* **2016**, *23*, 336–343. https://doi.org/10.1016/j.protcy.2016.03.035.
48. Hao, L.; Lawrence, J. Effects of CO_2 laser irradiation on the wettability and human skin fibroblast cell response of magnesia partially stabilised zirconia. *Mater. Sci. Eng. C* **2003**, *23*, 627–639. https://doi.org/10.1016/S0928-4931(03)00056-0.
49. Teughels, W.; Van Assche, N.; Sliepen, I.; Quirynen, M. Effect of material characteristics and/or surface topography on biofilm development. *Clin. Oral Implant. Res.* **2006**, *17*, 68–81. https://doi.org/10.1111/j.1600-0501.2006.01353.x.
50. Callow, M.E.; Fletcher, R.L. The influence of low surface energy materials on bioadhesion a review. *Int, Biodeterior. Biodegradation* **1994**, *34*, 333–348. https://doi.org/10.1016/0964-8305(94)90092-2.
51. Sendi, P.; Banderet, F.; Graber, P.; Zimmerli, W. Periprosthetic joint infection following staphylococcus aureus bacteremia. *J. Infect.* **2011**, *63*, 17–22. https://doi.org/10.1016/j.jinf.2011.05.005.
52. Wang, R.; He, X.; Gao, Y.; Zhang, X.; Yao, X.; Tang, B. Antimicrobial property, cytocompatibility and corrosion resistance of Zn-doped ZrO_2/TiO_2 coatings on Ti6Al4V implants. *Mater. Sci. Eng. C* **2017**, *75*, 7–15. https://doi.org/10.1016/j.msec.2017.02.036.

53. Bannunah, A.M. Biomedical Applications of Zirconia-Based Nanomaterials: Challenges and Future Perspectives: A review. *Molecules* **2023**, *28*, 5428. https://doi.org/10.3390/molecules28145428.